

## THz Generation from Plasmonic Nanoparticle Arrays

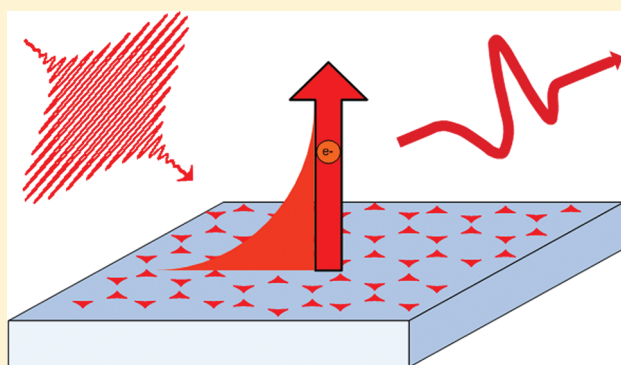
D. K. Polyushkin, E. Hendry, E. K. Stone, and W. L. Barnes\*

School of Physics and Astronomy, Exeter EX4 4QL, United Kingdom

S Supporting Information

**ABSTRACT:** We investigate the generation of THz pulses when arrays of silver nanoparticles are irradiated by femtosecond laser pulses, providing the first reproducible experimental evidence in support of recent theoretical predictions of such an effect. We assess our results in the context of a model where photoelectrons are produced by plasmon-mediated multiphoton excitation, and THz radiation is generated via the acceleration of the ejected electrons by ponderomotive forces arising from the inhomogeneous plasmon field. By exploring the dependence of the THz emission on the femtosecond pulse intensity and as a function of metal nanoparticle morphology, and by comparing measurements to numerical modeling, we are able to verify the role of the particle plasmon mode in this process.

**KEYWORDS:** Terahertz, plasmon, nanoparticle, photoemission



The fields of nanophotonics, near-field optics and plasmonics all seek to harness light at the subwavelength scale. Plasmonics in particular offers the prospect of deep subwavelength confinement of light and an associated enhancement of the electromagnetic field strength. These attributes enable an increasing number of applications to be pursued, ranging from data storage,<sup>1</sup> to therapies for cancer,<sup>2</sup> and the generation of deep-UV/soft X-rays by high-harmonic generation.<sup>3</sup>

While many applications exploit the spatial confinement and field enhancement in the vicinity of plasmonic metal nanostructures, much less attention has been given to the field enhancement that occurs inside the metal. One phenomenon that hinges on this effect is the photoemission of electrons from nanostructured metals after excitation by ultrashort laser pulses. Several studies have investigated such ultrafast photoemission from planar films,<sup>4</sup> islandised metal films<sup>5</sup> and metallic gratings.<sup>6,7</sup> In each of these studies, plasmon modes associated with the metal surfaces have been suggested as being involved in the photoemission process. It is thought that the role of the plasmon is 2-fold: high electric fields inside the metal can be used to explain observed enhancements in photoemission after excitation on resonance with plasmon modes, while high field gradients are thought to induce charge acceleration, through the ponderomotive force,<sup>8</sup> giving rise to high energy photoelectrons.<sup>9</sup>

Such a rapid burst of high energy photoelectrons could possibly be accompanied by the emission of THz radiation. THz emission following the illumination of nanostructured metal surfaces by femtosecond laser pulses has been observed from planar (rough) metal films,<sup>10–12</sup> and corrugated films (gratings).<sup>13,14</sup> Various mechanisms for the THz emission have been proposed including optical rectification<sup>12</sup> and photoemission.<sup>13</sup> Here we provide the first reproducible experimental evidence that supports the recent

predictions<sup>15</sup> of THz emission from metallic nanoparticles. We investigate two sample types, semicontinuous metal films and ordered arrays of metal nanoparticles. The semicontinuous films exhibit more intense THz emission. However, owing to the inhomogeneous nature of these metallic nanostructures, they are not an easy platform upon which to explore the underlying physics. Ordered arrays of metallic nanoparticles allow us to overcome this problem since these structures have the important advantage that their electromagnetic response can be modeled in detail. By exploring the dependence of the THz emission as a function of metal nanoparticle morphology and dimensions, and by comparing measurements to electromagnetic modeling, we are able to confirm the role of particle plasmon modes in the THz emission process.

The semicontinuous films are fabricated by evaporation of metal under vacuum onto glass substrates at a deposition rate of  $\sim 0.1 \text{ nm s}^{-1}$ , at a pressure of  $< 10^{-5} \text{ mbar}$ . For low ( $< 20 \text{ nm}$ ) film thicknesses the metal does not properly wet the substrate (glass) surface and so a continuous film does not form, instead surface tension leads to the formation of metal islands.<sup>16</sup> Sample morphology is characterized by scanning electron microscopy (SEM), and the linear optical response assessed by acquiring extinction spectra. Examples of extinction spectra and of SEM images are shown in Figure 1. A range of samples were made, using both silver and gold, and altering the mass of metal deposited. We refer to the different films by their mass thickness, the equivalent thickness of metal that would have been produced had the film been continuous. Ordered arrays of metallic nanoparticles are

**Received:** July 15, 2011

**Revised:** October 13, 2011

**Published:** October 18, 2011

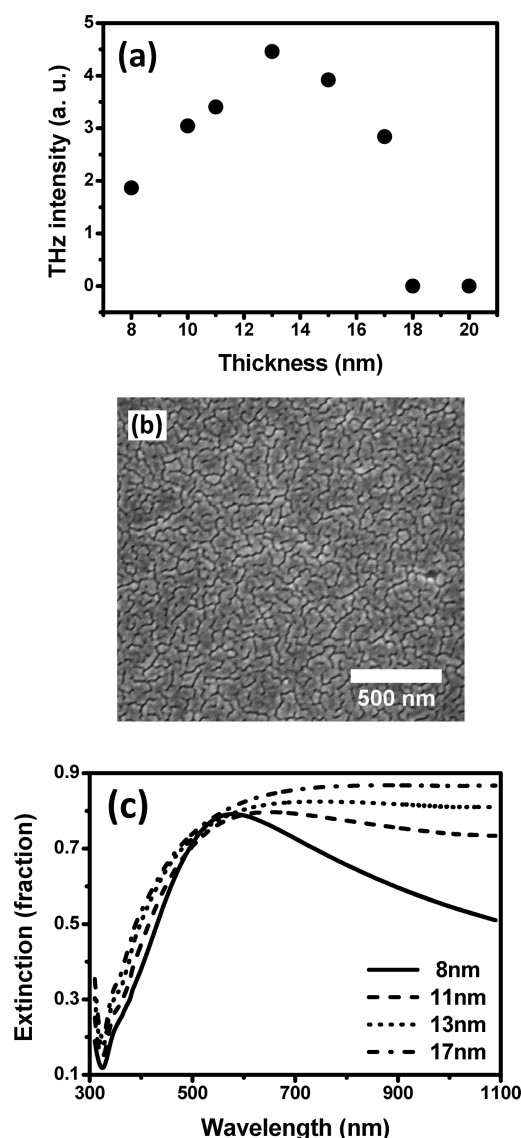


**Figure 1.** Top (a) Measured THz intensity from semicontinuous silver films as a function of the mass thickness of the film. Middle (b) SEM picture of percolating silver film, mass thickness 12 nm (the darkest regions indicate the absence of metal), scale bar is 500 nm. Lower (c) extinction spectra of silver films of a number of different mass thicknesses.

produced using nanosphere lithography (NSL).<sup>17</sup> The NSL technique allows for the facile production of large area ( $\sim 1 \text{ cm}^2$ ) nanoparticle arrays. Briefly, clean glass substrates are submerged in ultrapure deionized water. A suspension of colloidal nanospheres is then introduced onto the water surface, and the nanospheres self-assemble into a hexagonally close-packed monolayer array. When transferred to a substrate, and when the water has evaporated, this monolayer may be used as a lithographic mask through which to deposit metal by thermal evaporation. Finally the polystyrene nanospheres are removed by ultrasonication in toluene to leave a honeycomb array of triangular particles. NSL samples are characterized using SEM, while extinction spectra are acquired using microspectroscopy to probe sample areas of order several micrometers squared. Figure 2 shows examples of extinction spectra and an example SEM image for the NSL arrays.

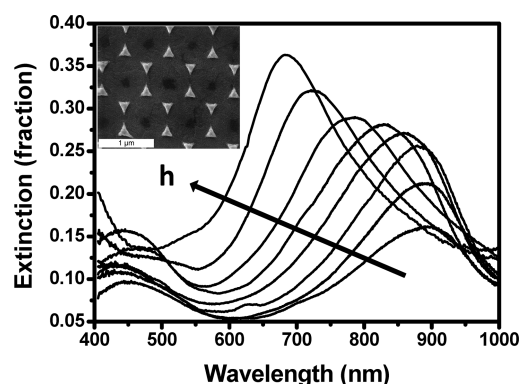


**Figure 2.** Optical extinction spectra from nanosphere lithography (NSL) arrays of triangular particles of various thicknesses (heights). The bead size of the template was 780 nm. Data are shown for particle heights (*h*) of 20, 30, 40, 50, 60, 70, 100, 150 nm. The arrow shows the direction of increasing particle height. Inset: scanning electron microscope image of one array.

For the THz measurements we employ  $\sim 100$  fs amplified laser pulses with a central wavelength of 800 nm. The pulses are split into two beams, one for THz generation and one for detection of the emitted THz radiation. The generation beam, once focused to a spot of diameter 1 mm, has energy densities up to  $9 \text{ mJ cm}^{-2}$ , corresponding to peak intensities up to  $90 \text{ GW cm}^{-2}$ . THz radiation is collected by mirrors and focused onto a 1 mm thick ZnTe 110-oriented electro-optical crystal.<sup>18</sup> The THz field induces birefringence in the crystal, and this induced birefringence modifies the polarization state of the 800 nm detection pulse that is coincident with the THz pulse on the crystal. The change in polarization state is measured using a polarizing beam splitter and a pair of balanced photodiodes. A quarter waveplate placed before the polarizer is used to ensure the polarization states are balanced when no THz field is present. The delay of the pump with respect to the THz pulses is achieved with a delay line. The spectrum of the generated THz radiation is obtained through Fourier transformation of the time-domain signal. The signals are in the  $\sim 1$  THz range owing to the duration of the excitation pulses we employ. Typical frequency-domain and time-domain signals from an NSL array of silver nanoparticles are shown in Figure 3.

Figure 1a shows the measured THz intensity as a function of mass thickness of a number of silver semicontinuous metal films; the intensity of the generation beam was  $5 \text{ GW cm}^{-2}$ , and the sample was illuminated at an angle of  $\sim 40^\circ$ . We can see that the THz emission is a maximum for mass thicknesses of  $\sim 13$  nm. We observe a similar dependence for gold samples (not shown) with a peak at a mass thickness of  $\sim 10$  nm. It is interesting to note that for both silver and gold the strongest THz signal occurs for near the percolation threshold (i.e., samples for which the islands become connected rather than isolated); the percolating nature of these samples was confirmed via resistivity measurements. We correlate these observations with the associated extinction spectra from the samples. The extinction spectra, Figure 1c, only show particle plasmon resonances for mass thicknesses below 11 nm for silver (and below 9 nm for gold). Why then does the THz signal continue to increase in strength even for percolating structures? Although the extinction spectra corresponding to percolating samples do not show a well-defined plasmonic resonance, this does not mean that plasmonic resonances are not

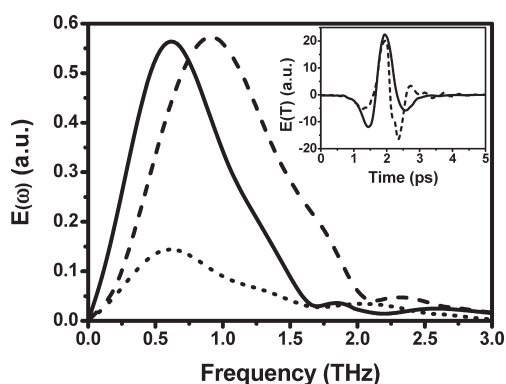


**Figure 3.** Spectra of the emitted THz pulse after optical excitation of NSL arrays made using spheres of diameter 390 nm (dotted line) and 780 nm (solid line), both with particles of thickness (height) 60 nm. Also shown for comparison is the emission (from optical rectification) of a 1 mm thick ZnTe crystal (scaled down by factor 100) (dashed line). Inset: time-domain measurement of the emitted THz pulse for 780 nm NSL sample (solid line) and ZnTe (dashed line), the electric field strength is shown as a function of time.

present.<sup>19</sup> Examination of the SEM images for the different samples indicates that the percolating structures have many small gaps: it is probable that the high-field enhancements associated with such gaps<sup>20</sup> are responsible for the high THz signal. Similar results have very recently been obtained by Ramakrishnan and Planken,<sup>12</sup> they too find a maximum in THz emission when their gold films are percolating rather than islandised.

The electric field strength of the THz pulses emitted by these samples upon irradiation is rather high: the maximum THz pulse field strength is only a factor  $\sim 10$  smaller than pulses generated by optical rectification in a 1 mm thick ZnTe crystal using similar excitation intensities, despite a film thickness that is 5 orders of magnitude less than the crystal. If optimized, particle plasmon structures may therefore be practical as emitters in THz applications, especially where local THz emitters would be beneficial.

To optimize the effect, one needs to be able to correlate THz emission with sample morphology, and in particular to be able to determine local field enhancements. This is very difficult for semicontinuous films, but this difficulty can be overcome if we investigate well-defined, ordered nanoparticle arrays. The spectral position of the plasmon modes supported by metallic nanoparticle arrays can be controlled by varying the size, height, and spacing of the metallic nanoparticles. As is the case for the semicontinuous films, extinction spectra allow us to monitor the plasmon modes supported by the different particle array structures we fabricate (Figure 2). The largest peak extinction (Figure 2) corresponds to the dipolar plasmon resonance of the particles.<sup>21</sup> THz signals are shown in Figure 3 from two different NSL samples. These samples differ only in the size of the polystyrene beads used to create the lithographic mask: beads of 390 and 780 nm were used, corresponding to arrays which exhibit plasmon resonances at  $\sim 550$  and  $\sim 830$  nm, respectively. The data in Figure 3 show that the amplitude of the THz signal from the sample with a plasmon resonance at  $\sim 830$  nm is approximately four times stronger than that from the sample with a plasmon resonance at  $\sim 550$  nm, the samples were illuminated with the same incident intensity,  $\sim 5 \text{ GW cm}^{-2}$ . These results suggest that THz emission is enhanced when the wavelength of the plasmon resonance matches the incident wavelength.

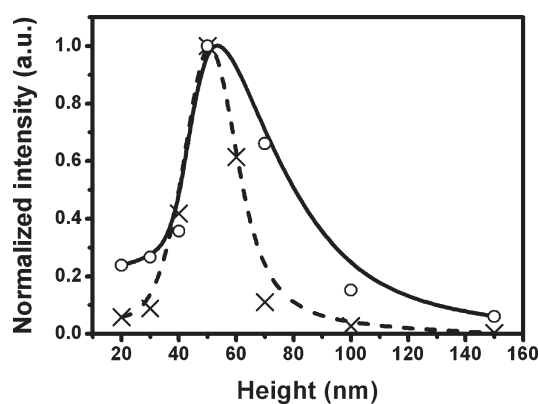


**Figure 4.** Dependence of THz intensity on the thickness (height) of particles made by using spheres with diameter 780 nm. Two sets of data are shown, (full line, open circles) are for normally incident excitation, (dashed line, crosses) are for oblique excitation at an angle of  $40^\circ$ . The lines are included solely as guides the eye. The incident intensity in both cases was  $\sim 5 \text{ GW cm}^{-2}$ .

To further explore this relationship between plasmon resonance and THz emission, we created a range of different nanoparticle arrays. Each was produced using the same diameter polystyrene spheres (780 nm), differing only in the thickness of the silver deposited. Changing the thickness (height,  $h$ ) of the particles results in a shift of the plasmon resonance.<sup>22</sup> Extinction spectra for arrays with thicknesses of silver in the range 20–150 nm are shown in Figure 2. The spectra indicate that the plasmon resonance for the short particles (height  $\sim 20$  nm) is at  $\sim 900$  nm, on the long wavelength side of the illumination wavelength ( $\sim 800$  nm). As the height of the particles is increased the resonance shifts to shorter wavelengths. For particles  $\sim 60$  nm height, the resonance wavelength matches the wavelength of the incident pulses. The intensity of the THz emission is shown as a function of particle thickness (height) in Figure 4. Two sets of data are shown, one set was obtained for pulses normally incident on the array, the other for pulses incident at an oblique angle of  $\sim 40^\circ$  (as discussed below, the THz emission is much stronger when samples are illuminated away from normal incidence). We observe in both data sets a maximum THz emission for arrays with particle height (thickness)  $\sim 50$  nm, close to the condition of resonant excitation. This implies that the excitation of the particle plasmon resonance by the incident laser pulse enhances the THz emission process.

In order to gain insight into the physical origins of this observed height dependence of the THz emission, we carried out electromagnetic modeling<sup>23,24</sup> using the finite element method (HFSS v.13, Ansoft Corporation). Our three-dimensional model employs the rhombic unit cell of the arrays, as shown in Figure 6. Spatial dimensions for the unit cell and the particles are taken from SEM images. The model employs  $\sim 15\,000$  tetrahedral elements per particle, and solutions were sought following adaptive procedures to optimize the meshing. Particle edges were rounded to a radius of 3 nm. Note that the substrate was excluded in our model since its presence leads to the existence of propagating diffracted orders that significantly complicates the calculation, making convergence too computationally intensive for the available computing resources. Both reflection spectra and the spatial distribution of the field strength were calculated (using a frequency dependent permittivity for silver<sup>25</sup>), the average field enhancement is calculated by normalizing

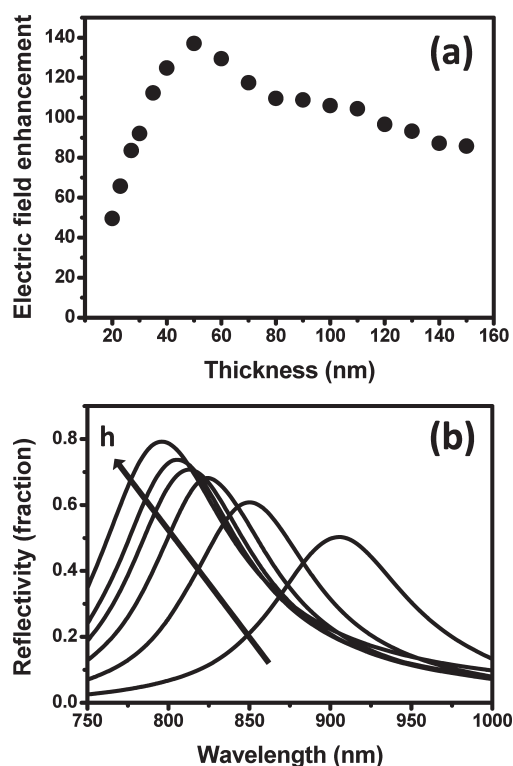


**Figure 5.** Results from numerical modeling. Upper panel (a): the dependence of the maximum field enhancement (located close to the facing tips) on particle thickness (height). Lower panel (b): shows how the calculated reflection spectra change with varying particle height. Data are shown for heights of 20, 30, 40, 50, 60, 90 nm, and the arrow shows the direction of increasing particle height.

to the incident field strength. Our calculations (Figure 5) indicate that the optimum particle height in terms of field enhancement occurs when the plasmon resonance is close to the incident wavelength. Closer inspection of the data shows that maximum extinction seems to be slightly red-shifted with respect to the maximum THz signal (near-field enhancement). More specifically, the particle height of 50 nm gives the greatest THz signal strength (Figure 5a), and for this particle height the extinction peaks at 810 nm, whereas the pump is centered at 800 nm. This shift appears more strongly in the experimental data. Again the particle height of 50 nm gives the strongest THz signal when pumped at 800 nm, see Figure 4, but for this particle height the extinction peaks at 860 nm, see Figure 2. This shift is of the opposite sign to that seen in fluorescence enhancement studies.<sup>26,27</sup>

It is possible that the sign of the shift depends on the shape of the particle,<sup>28</sup> but this aspect needs further investigation to clarify the physics behind the shift we observe. The local electric field is inhomogeneous, the regions of high enhancement are strongly localized at the vertices of the particles, and predominantly along the polarization axis of the illumination. However, due to the symmetry of the unit cell, the field enhancement exhibits a center of symmetry in space. As discussed later, this symmetry plays an important role in the emission process.

An important trend is clear from our numerical modeling. The highest field enhancements are generated both inside and outside the particles corresponding to the samples from which we observe the highest THz emission; an example of the calculated field enhancement distribution is shown in Figure 6. The plasmon

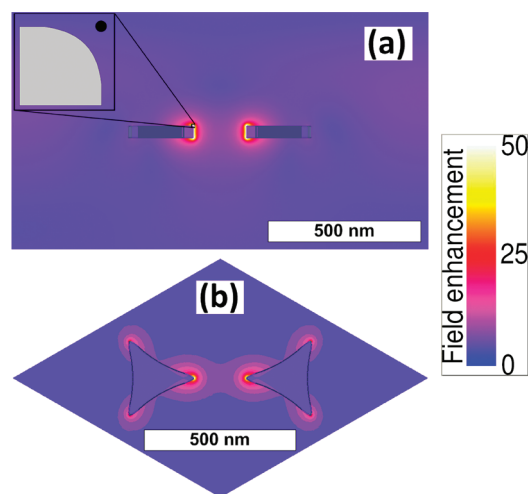


**Figure 6.** Field distributions for a 40 nm thick pair of particles in a rhombic unit cell calculated using finite element modeling, illuminated with a wavelength of 800 nm. (a) Cross-section, (b) slice through center of plane of array. The E-field of the illuminating light is parallel to the line joining the particles. The point at which the field is calculated is shown in the inset to (a). The field is calculated in the plane parallel to the upper (flat) surfaces of the particles at the point where the corner of one of them would have been had rounding of the tip not been implemented. The plots show the time-averaged magnitude of the electric field.

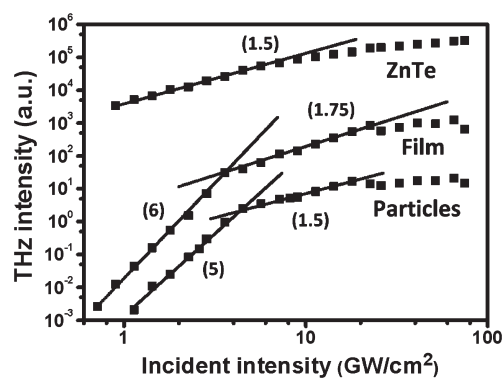


**Figure 7.** Emitted THz fluence as a function of the optical excitation intensity for (lower data set) an NSL array produced using spheres of diameter 780 nm, and 50 nm silver layer; (middle data set) a percolating silver film of equivalent mass thickness 15 nm; and (upper data set) optical rectification of ZnTe. The numbers in the brackets are the fitted “orders” of the lines associated with the data.

clearly plays an important part in the emission process. However, the precise role that plasmon excitation plays is still not clear. To address this point, let us now turn to the dependence of the THz emission on the intensity of the incident pulses. In Figure 7, we plot the emitted THz intensity as a function of the optical excitation intensity for an NSL array made using spheres of diameter 780 nm with silver particles of height 50 nm (particles); for semicontinuous silver films (film); and for ZnTe (ZnTe). The THz intensity from the ZnTe shows an  $\sim 2$ nd order dependence on the pump intensity as expected (the dependence is somewhat subsecond order, as has been observed by others<sup>29</sup>). For incident optical intensities  $< 5$  GW/cm<sup>2</sup>, the THz intensity shows an  $\sim 5$ th ( $\sim 6$ th) order dependence on the optical pulse intensity for the NSL particles (semicontinuous films), dropping



to <2nd order for intensities in the range  $\sim 5$  to  $\sim 20$  GW cm $^{-2}$ . For optical intensities  $>20$  GW cm $^{-2}$  our samples undergo ablation. It is important to note that for incident optical intensities  $<5$  GW cm $^{-2}$  the dependence is significantly different from the more common second order THz generation mechanisms such as optical rectification<sup>18</sup> (an example from optical rectification is also shown in Figure 7 for a ZnTe crystal). However, similar bimodal intensity dependences have also been observed in ultrafast photoemission measurements.<sup>5</sup> For example, the order of the intensity dependence of the photocurrent exhibited by a flat silver surface excited by femtosecond pulses in the Kretschmann–Raether geometry was observed to vary from  $\sim 3$  for intensities  $<4$  GW cm $^{-2}$  to  $\sim 1.5$  for intensities  $>8$  GW cm $^{-2}$ .<sup>29</sup> This suggests a link between photoemission and THz generation. Indeed, the order parameter for the generation of THz radiation from a one-dimensional diffraction grating in gold has been observed to vary from 5.0 to 3.5 on increasing the intensity of photoexcitation over a similar range.<sup>13</sup> We note that the recent work of Ramakrishnan and Planken on semicontinuous gold films does not show a bimodal intensity dependence; however, their conditions were somewhat different, notably they used a lower pump intensity but a higher average power.

Many of the main properties of the measured THz emission (such as the unusual intensity dependence shown in Figure 7) can be accounted for within the following model, based upon that of Welsh et al.:<sup>13</sup>

- (i) Particle-plasmon excitation and multiphoton absorption of light leads to enhanced electromagnetic fields around the particle and to the ejection of electrons from the metal.
- (ii) The ejected electrons are subject to forces exerted on them by the electromagnetic field; in our case this is primarily the field enhanced by the particle plasmon resonance.
- (iii) Since the electromagnetic field associated with the plasmon resonances is localized in the close vicinity of the particles the field is inhomogeneous. This inhomogeneity leads to ponderomotive acceleration of the electrons.<sup>30</sup> The time scale of this acceleration is slow with respect to the optical period of the pump light and is determined by the spatial variation in the field. Moreover, the pulsed nature of the incident light means that the ponderomotive motion produces a time varying current. The duration of the pulse ( $\sim 100$  fs) means that the frequency of the ensuing radiation is of order THz.

Before considering our model further one might question whether electrons ejected from the metal can propagate far enough for them to produce the currents responsible for the THz emission as invoked in the model outlined above, their propagation will be limited by scattering from air molecules. Ejected electrons need to be able to travel distances of order  $\sim 20$  nm in air without being scattered, this is the length scale of the field localization around the nanoparticles (see Supporting Information). Scattering by air molecules of electrons having energies in the range 0.1–1000 eV will be dominated by scattering due to N<sub>2</sub>, for which the maximum scattering cross-section in this energy range is<sup>31</sup>  $\sim 30 \times 10^{-20}$  m<sup>2</sup>. The number density of air molecules at STP is  $\sim 3 \times 10^{25}$  m $^{-3}$ , thus the total cross-section in 1 m<sup>3</sup> is  $\sim 10^7$  m $^{-1}$ . The thickness of air required to give unit cross-section is thus  $10^{-7}$  m, that is, 100 nm. This is greater than the typical decay length of the plasmon field, 20 nm, the distance over which ponderomotive action will take place.

Returning now to the model discussed above, full details of our model are given in the Supporting Information. In brief, we postulate that the photocurrent is proportional to the product of the photoelectron number and the acceleration of these photoelectrons. We then consider the intensity dependence of photo-generated electrons under different regimes of photoexcitation (multiphoton ionization and tunnelling ionization). Acceleration is assumed to be due to spatial inhomogeneities in the local electric fields, resulting in ponderomotive action. In this picture, a THz pulse is generated due to a time varying photocurrent, an effect arising from the finite temporal width of the excitation pulses. This model contains a number of key assumptions. First, for simplicity, the ponderomotive potential generated by the plasmonic field is regarded as being uniform in the plane of the substrate. Second, when considering intensity dependences we use the peak power of the femtosecond pulses (i.e., we neglect the change in the incident intensity during the pulse envelope). Although approximate for low incident intensities,  $<1$  GW cm $^{-2}$ , our model predicts that the THz fluence will have an eighth order dependence on the incident intensity. Above 1 GW/cm $^{-2}$  the model predicts a sixth–eighth order dependence, owing to saturation of the ponderomotive force. A third regime is predicted above 10 GW cm $^{-2}$ , here the dependence is predicted to be second order, as tunneling ionization rather than multiphoton excitation takes over as the mechanism by which electrons are liberated from the metal. We do not expect exact agreement between the simple model and our experiments: as shown in our numerical modeling, the local electromagnetic fields is spatially inhomogeneous, something we greatly simplified in our model. Moreover, local surface roughness will influence both the electron trajectories<sup>9</sup> and the work function.<sup>32</sup> Thus, in the experiment the enhancement factor will be highly inhomogeneous in the plane of the substrate. Furthermore, we assume a single frequency for the incident pump light; the pulse width (100 fs) has a spread of  $\sim 20$  nm, significantly less than the  $\sim 100$  nm width of the plasmon resonances.

How do the results of this model compare with our results? First, the model predicts an 8th order dependence of the THz fluence on the incident intensity at low incident intensities, something that we do not observe (Figure 7). We can understand why we do not see this 8th order dependence as follows. In our experiment we were not able to acquire low-noise data for incident intensities below  $<1$  GW cm $^{-2}$ , thus the low intensity regime in which the ponderomotive force is unsaturated and where an 8th order dependence is expected, is not available to us. It is interesting to note that the cross over between  $\sim 6$ th and  $\sim 2$ nd order dependences in our experiment ( $\sim 5$  GW cm $^{-2}$  in Figure 7) occurs at approximately the intensity predicted for the transition between multiphoton to tunnelling regimes in our simple model,  $\sim 10$  GW cm $^{-2}$ . This is strong evidence that the THz emission measured from our metallic particles is linked to the rapid burst of accelerated photoelectrons initiated by the ultrafast laser pulses.

Even though each particle generates a pulse of electrons, the radiative THz emission for our samples will be determined by the entire array of particles. An understanding of how the electromagnetic fields generated by single particles add up in the far field is thus needed. Owing to the centrosymmetric nature of our arrays, the radiation emitted due to local ponderomotive currents in the plane of the substrate will cancel in the far-field. Therefore only components of the ponderomotive currents out-of-plane can contribute to THz emission. This effect can be observed in

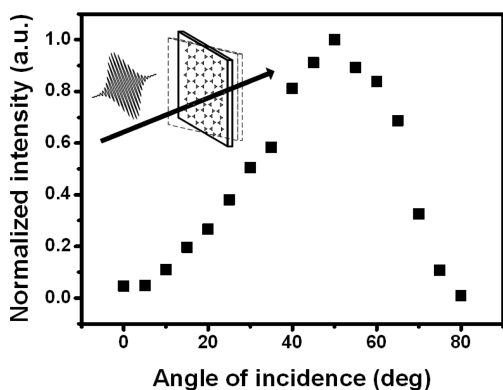


**Figure 8.** Intensity of emitted THz generation as function of angle of incidence of optical pulses. The sample was made via the NSL technique, using 780 nm spheres, the silver was 50 nm thick, and the incident laser power was  $15 \text{ GW cm}^{-2}$ . The inset shows the nature of the oblique illumination. Normal incidence corresponds to an angle of zero degrees.

Figure 8, where we plot the THz intensity (measured in the direction of the excitation beam) as a function of the polar angle of incident light. For normal incidence, due to the absence of any phase retardation between the excitation of different particles, ponderomotive currents are not radiative and we should thus not expect THz emission. In the experiment, we observe a small residual THz emission at normal incidence, most likely due to inhomogeneities in the NSL arrays and/or the finite size of the excitation beam. Away from normal incidence, the THz emission increases. We stress that this effect has nothing to do with angle dependence of the field enhancement (indeed, our modeling suggests that the local field enhancement falls as one illuminates away from normal incidence). In our experiments, we observe a maximum in the THz emission from all arrays for incident angles between 40 and 60°. One can qualitatively understand the origin of this maximum; as the angle of incidence increases, the magnitude of the out-of-plane component of the ponderomotive current capable of contributing to radiative emission increases as  $\sin(\theta)$ . In combination with this effect, sample rotation also increases the illuminated area of the sample and reduces the effective excitation intensity. One therefore expects the emitted THz radiation to scale as  $\cos^n(\theta)$ , where  $n$  represents the order of the THz (intensity) emission process. In this simple picture, the intensity of THz radiation is expected to scale as  $\cos^n(\theta) \times \sin(\theta)$ . One should note that such a simple picture is not complete as it ignores, for example, the angle dependent coupling of the incident light to the particle plasmon resonances. It does however suggest that there will be an optimum angle for THz generation away from normal incidence, as seen in our experiments.

In conclusion, we have investigated the generation of THz pulses via irradiation of arrays of silver nanoparticles with femto-second laser pulses. Our observations are consistent with a model in which THz radiation is produced by the emission of photoelectrons through multiphoton excitation and subsequent acceleration of these emitted electrons by ponderomotive forces associated with the optical fields of the plasmons in the metallic nanostructures. The magnitude of the THz emission is remarkably large for an essentially 2D metamaterial, arising from an effective nonlinear polarization which is up to 4 orders of magnitude higher than in dielectric materials such as ZnTe. There is therefore considerable scope to design 3D arrays of metallic nanoparticles, that is, metamaterials specifically designed to give

optimal THz emission. As noted above, the centrosymmetric nature of our arrays means that THz radiation emitted due to local ponderomotive currents in the plane of the substrate will cancel in the far-field, designs employing noncentrosymmetric particles need to be investigated. Furthermore, attention to maximizing the field enhancement through particle design, and perhaps array design, where collective resonances<sup>33</sup> may play a role, are other avenues for future exploration. Finally we note that with some optimization it is plausible that one could use a single metallic nanoparticle as a local THz emitter.

## ■ ASSOCIATED CONTENT

**S Supporting Information.** Details of the model we used to explore the dependence of the THz fluence on the incident optical intensity are contained in the Supporting Information. This material is available free of charge via the Internet at <http://pubs.acs.org>.

## ■ AUTHOR INFORMATION

### Corresponding Author

\*E-mail: [w.l.barnes@exeter.ac.uk](mailto:w.l.barnes@exeter.ac.uk).

## ■ ACKNOWLEDGMENT

This work is supported in part by the EPSRC (EP/F026757). E.H. is supported by a RCUK Fellowship. The authors wish to acknowledge F. J. Garcia de Abajo for the calculation concerning electron propagation in air.

## ■ REFERENCES

- (1) Zijlstra, P.; Chon, J. W. M.; Gu, M. *Nature* **2009**, *459*, 410–413.
- (2) Loo, C.; Lowery, A.; Halas, N.; West, J.; Drezek, R. *Nano Lett.* **2005**, *5*, 709–11.
- (3) Kim, S.; Jin, J.; Kim, Y.-J.; Park, I.-Y.; Kim, Y.; Kim, S.-W. *Nature* **2008**, *453*, 757–60.
- (4) Irvine, S.; Dombi, P.; Farkas, G.; Elezzabi, A. *Phys. Rev. Lett.* **2006**, *97*, 146801.
- (5) Gloskovskii, A.; Valdaitsev, D.; Cinchetti, M.; Nepijko, S.; Lange, J.; Aeschlimann, M.; Bauer, M.; Klimenkov, M.; Viduta, L.; Tomchuk, P.; Schönhense, G. *Phys. Rev. B* **2008**, *77*, 195427.
- (6) Kupersztych, J.; Monchicourt, P.; Raynaud, M. *Phys. Rev. Lett.* **2001**, *86*, 5180–5183.
- (7) Kupersztych, J.; Raynaud, M. *Phys. Rev. Lett.* **2005**, *95*, 147401.
- (8) Boot, H.; Harvie, R. *Nature* **1957**, *180*, 1187.
- (9) Rácz, P.; Irvine, S. E.; Lenner, M.; Mitrofanov, A.; Baltuška, A.; Elezzabi, A. Y.; Dombi, P. *Appl. Phys. Lett.* **2011**, *98*, 111116.
- (10) Kadlec, F.; Kuzel, P.; Coutaz, J.-L. *Opt. Lett.* **2004**, *29*, 2674–6.
- (11) Kadlec, F.; Kuzel, P.; Coutaz, J.-L. *Opt. Lett.* **2005**, *30*, 1402–4.
- (12) Ramakrishnan, G.; Planken, P. C. M. *Opt. Lett.* **2011**, *36*, 2572–4.
- (13) Welsh, G.; Hunt, N.; Wynne, K. *Phys. Rev. Lett.* **2007**, *98*, 026803.
- (14) Welsh, G. H.; Wynne, K. *Opt. Express* **2009**, *17*, 2470–80.
- (15) Gao, Y.; Chen, M.-K.; Yang, C.-E.; Chang, Y.-C.; Yin, S.; Hui, R.; Ruffin, P.; Brantley, C.; Edwards, E.; Luo, C. *J. Appl. Phys.* **2009**, *106*, 074302.
- (16) Kümmerlen, J.; Leitner, A.; Brunner, H.; Aussenegg, F.; Wokaun, A. Enhanced dye fluorescence over silver island films: analysis of the distance dependence. *Mol. Phys.* **1993**, *80*, 1031–1046.
- (17) Hulteen, J. C.; Van Duyne, R. P. *J. Vac. Sci. Technol., A* **1995**, *13*, 1553.
- (18) Nahata, A.; Welington, A. S.; Heinz, T. F. *Appl. Phys. Lett.* **1996**, *69*, 2321.

- (19) Wustholz, K. L.; Henry, A.-I.; McMahon, J. M.; Freeman, R. G.; Valley, N.; Piotti, M. E.; Natan, M. J.; Schatz, G. C.; Van Duyne, R. P. *J. Am. Chem. Soc.* **2010**, *132*, 10903–10.
- (20) García-Vidal, F.; Pendry, J. *Phys. Rev. Lett.* **1996**, *77*, 1163–1166.
- (21) Kelly, K. L.; Coronado, E.; Zhao, L. L.; Schatz, G. C. *J. Phys. Chem. B* **2003**, *107*, 668–677.
- (22) Jensen, T. R.; Malinsky, M. D.; Haynes, C. L.; Van Duyne, R. P. *J. Phys. Chem. B* **2000**, *104*, 10549–10556.
- (23) Parsons, J.; Burrows, C. P.; Sambles, J. R.; Barnes, W. L. *J. Mod. Opt.* **2010**, *57*, 356–365.
- (24) Murray, W. A.; Suckling, J. R.; Barnes, W. L. *Nano Lett.* **2006**, *6*, 1772–7.
- (25) Lynch, D. W.; Hunter, W. R. In *Handbook of Optical Constants of Solids*; Palik, E. D., Ed.; Academic Press Inc.: New York, 1985; pp 275–367.
- (26) Thomas, M.; Greffet, J.-J.; Carminati, R.; Arias-Gonzalez, J. R. *Appl. Phys. Lett.* **2004**, *85*, 3863.
- (27) Chen, Y.; Munechika, K.; Ginger, D. S. *Nano Lett.* **2007**, *7*, 690–6.
- (28) Ru, E. C. Le; Etchegoin, P. G. *Principles of Surface-Enhanced Raman Spectroscopy and related plasmonic effects*, 1st ed.; Elsevier: New York, 2009.
- (29) Irvine, S. E.; Elezzabi, a Y. *Appl. Phys. Lett.* **2005**, *86*, 264102.
- (30) Eberly, J. H.; Javanainen, J.; Rzazewski, K. *Phys. Rep.* **1991**, *204*, 331–383.
- (31) Itikawa, Y. *J. Phys. Chem. Ref. Data* **2006**, *35*, 31.
- (32) Tsang, T.; Srinivasan-Rao, T.; Fischer, J. *Phys. Rev. B* **1991**, *43*, 8870.
- (33) Auguié, B.; Barnes, W. L. *Phys. Rev. Lett.* **2008**, *101*, 143902.